International Journal of Environmental Sciences
ISSN: 2229-7359
Vol. 11 No. 18s, 2025
https://theaspd.com/index.php

Atmosphere-Sensitive Reduction Of P-Nitrophenol Using B(PM-PP)/Zro$_2$ Nanocomposites: Toward Sustainable Electrochemical Reduction Platforms

P. Pon Maha lakshmi[1],[2]P. Rajakani[2], C.Vedhi[2]
[1] Research Scholar, Reg. No:21112232032007, Affiliated by Manonmaniam Sundaranar University, Abishekapatti, Tirunelveli - 627 012, Tamil Nadu, India.
[2] PG and Research Department of Chemistry, V. O. Chidambaram College, Tuticorin - 628 008, Tamil Nadu.

GraphicalAbstract:

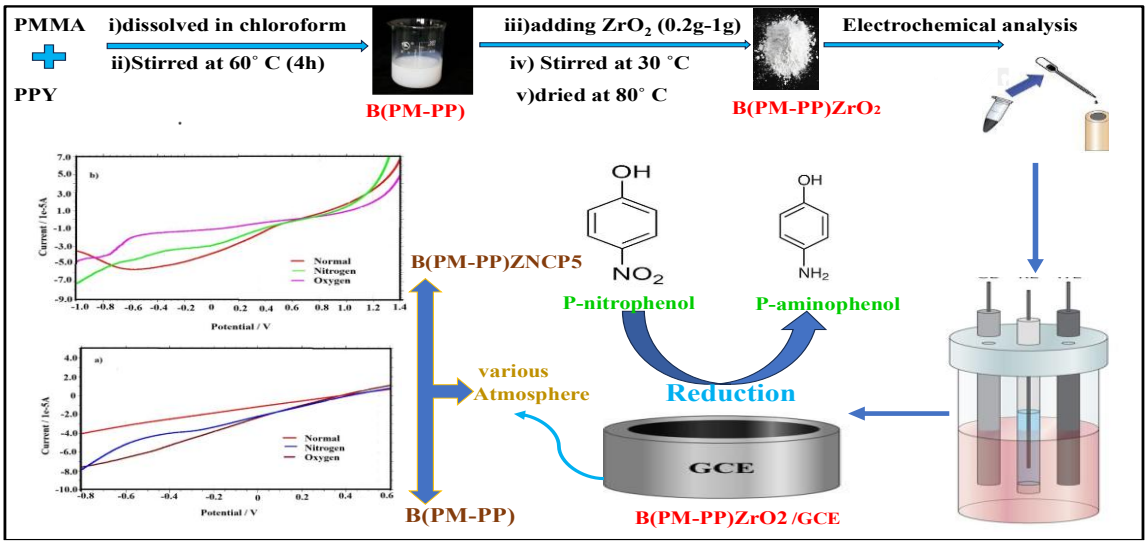

Highlights:

- Environmentally friendly polymer–metaloxide hybrid for nitrophenol reduction
- Tailored ZrO_2 content improves catalytic performance
- Oxygen atmosphere significantly enhances electron transfer
- Optimal performance achieved at 1 g ZrO_2 loading
- Promising for real-time pollutant reduction in environmental samples

Abstract

This study presents an eco-friendly platform for reduction of p-nitrophenol (PNP), utilizing a B(PM-PP)/ZrO_2 nanocomposite. Nanocomposites containing varying amounts of ZrO_2 (0.2,0.4,0.6,0.8,1.0 g) were synthesized. The interaction between the polymer blend and ZrO_2 has been confirmed by Fourier transform infrared spectroscopy (FTIR), as indicated by the Zr-O band at 840 cm $^{-1}$. The X-ray diffraction technique (XRD) was used to characterize the crystalline form of the nanocomposite. A high-resolution transmission electron microscopy (HRTEM) image demonstrates how each ZrO_2 particle embeds within the surface of the polymer blend component. Thermogravimetric analysis (TGA) was used to evaluate a thermal property of the nanocomposite. Cyclic voltammetry (CV) was used in electrochemical characterisation experiments to examine the enhanced performance of B(PM-PP)ZNCP5 modified GCE in optimal pH1.0 under various ambient conditions. In linear sweep voltammetry (LSV), B(PM-PP)ZNCP5 modified GCE potential moves to the negative side nearly 1000mV, demonstrating that the oxygen environment improved the electrocatalytic activity toward p-nitrophenol reduction. Using chromatoamperometric and chromatocoulometric studies, the diffusion coefficient value of B(PM-PP)ZNCP5/GCE, $3.14x10^6$ was determined under various atmospheric circumstances. As determined by electrochemical impedance spectroscopy (EIS), the resistance's double layer capacitance value is $5.573x10^6$ F/cm2. The findings underscore the potential of atmospheric-responsive reduction systems for environmental pollutant reduction.

1.INTRODUCTION

Persistent organic pollutants like p-nitrophenol are common in industrial wastewater and pose serious health and ecological threats. Efficient detection systems that are both cost-effective and environmentally conscious are urgently needed. The electrochemical approach has gained a lot of interest recently since it is inexpensive, highly efficient, and simple to use. Electrochemical techniques based on several chemically modified electrodes have been developed to determine p-nitrophenol.[1,2] According to Alan Omar et al [3], theoretical research is necessary to comprehend the identification and removal of 4-NP at the molecular level. Benzhi Liu et al reported Ag/MWCNT/GC electrode performs well as an electrocatalyst for p-nitrophenol reduction.[4] The catalytic efficiency of MoS2/ZnO for reducing 4-NitroPhenol to 4-AminoPhenol using Sodium borohydrate (NaBH4) was investigated using a simple exfoliation method. The rate constant of the reduction process was reported by Madhushree et al. [5] as 1.476 × 10^-4 min^-1. In the presence of PGMA@PAH@AuNPs, Maolin et al. studied the reduction of p-NP by NaBH4. The mechanism of the observed catalytic activity enhancement was suggested based on the large adsorption of p-nitrophenolate anions onto the positively charged spheres and the active epoxy groups of the polymer spheres.[6]According to Libo Sun et al.,[7] Au/P(ANI-co-Py) catalysts made using the sol adsorption process have a strong electronic metal-support interaction, suitable 4-NP adsorption, and a negatively charged Au NPs surface. This work provides very effective Au catalysts supported by conductive polymers. Conducting polymers, such as polypyrrole (PPY), beneficial characteristics, including high conductivity, strong biocompatibility, reversible redox characteristics, outstanding environmental stability, and ease of production.[8,9] while polymethyl methacrylate (PMMA) PMMA is used as a host matrix because of its superior chemical properties and amorphous thermoplastic, which is widely used because of its high impact strength, lightweight nature, resistance to shattering, and ease of processing[10]. Catalytic Behavior ZrO_2 shows Lewis acidity (can accept electrons), enabling, catalytic reduction or oxidation of target molecules.[11] Facilitation of proton-coupled electron transfer,[12] key in reactions like ORR or nitrophenol reduction,[13] chemically inert[14], thermally stable,[15] and biocompatible[16], Suitable for harsh environments and stable under electrochemical conditions.[17] Incorporating metal oxides like zirconium dioxide (ZrO_2) can improve overall reduction performance by enhancing conductivity and surface area.

This work explores how different concentrations of ZrO_2 within a PMMA-PPY blend influence reduction behavior, particularly under varied gaseous environments. Oxygen, as a reactive gas, is especially relevant due to its role in oxygen reduction reactions (ORR), which often complement electrochemical reduction.

2. MATERIALS AND METHODS

2.1.Reagents and Materials:

Methyl methacrylate (MMA) was purchased from Sigma-Aldrich, Potassium persulfate ($K_2S_2O_8$), Sodium dodecyl sulfate (SDS), pyrrole, ferric chloride, ZrO_2, and p-nitrophenol were all acquired from Merck. Chloroform and distilled water were used in the synthesis process.

2.2.Working electrode preparation

In our present investigation, a glassy carbon electrode modified with PB was used. It was made into PB solution by dissolving it in chloroform. Casting a single drop of PB solutions onto a surface and allowing the solvent to evaporate produced PB film. They were consequently rinsed with water and then transferred to an electrochemical cell for experimental purposes. A saturated calomel reference electrode (SCE), platinum wire counter electrode, and glassy carbon working electrode modified via PB were used in a three-electrode cell. Cyclic voltammogram of the PB-modified GCE immersed in 1.0 M H_2SO_4 at 27±2°C for 2 s. The gases used in these electrochemical investigations are N_2 and O_2. In these investigations, the standard condition (a saturated buffer absent of any other gases) is altered by constantly pumping N_2 or O_2 gas into the buffer solution via the cell's top for three minutes using a little tube. The tube is taken out of the solution throughout the process and left above the solution until the procedure is completed. Linear sweep voltammetry (LSV) has been recorded in 1.0 1.0 M H_2SO_4:1.0 M N-phenol (acidic Nitrophenol) on B(PM-PA) /GCE. It was carried out in normal as well as N_2 and O_2 saturated buffer at 50 mV/s. The above procedure is followed by ZrO_2/B(PM-PP) NCPs.

2.3. Characterization Techniques:

FT-IR spectra of the B(PM-PP) & ZrO_2/B(PM-PP) nanocomposites were recorded using a Nicolet iS5 FT-IR instrument in the frequency range of 400 to 4000 cm^{-1}. UV-Vis spectra of the solid samples were recorded on a JASCOV630 in the wavelength region 200 to 900nm. Powder X-ray diffraction patterns of the coatings were obtained by employing an XPERT-PRO diffractometer using CuKα (kα= 1.54060Å) radiation. The diffractometer was operated at 45kV and 30mA.To investigate the sample's thermal stability, the EXSTAR/6300 TGA instruments used thermal gravimetric analysis (TGA). High-resolution transmission electron microscopy (HR-TEM) was recorded on a JEM-3010 analysis using the morphology of the sample. Cyclic voltammetry(CV), studies were carried out at different pH, and Electrochemical impedance spectroscopy(EIS) was also experimented with using a CH Instrument (Model 650C) Electrochemical workstation.

3.Synthesis of polymer blend and nanocomposites

3.1. Polymerization of MMA

A simple procedure was followed to prepare PMMA, which involved placing 0.1M of MMA, 0.01M of SDS was added in 60 ml of distilled water in a 250ml round bottom flask, and the solution was stirred for 1h at 75°C. 0.001M of $K_2S_2O_8$ (initiator) dissolved in water was added gradually, drop by drop, and stirred for ½ hour at 80°C. The solution was then filtered, washed, and finally dried at 100°C for 24h under a vacuum to yield PMMA solid material.

3.2. Polymerization of pyrrole

0.1M pyrrole monomer was rapidly added to distilled water along with 0.1M potassium persulfate and 0.1M ferric chloride; vigorous magnetic stirring was continued to aid in the pyrrole's dispersion. At a temperature of 25°C, the polymerization process was carried out for 4 hours. Fine black particles began to precipitate very instantly. The synthesized PPy was filtered from the solution using filter paper after the allotted polymerization duration, and it was repeatedly and carefully cleaned with distilled water and ethanol before being dried overnight at around 40°C in a vacuum oven.

3.3. Synthesis of PMMA-PPY blends

PMMA and PPY 2:1 ratio was dissolved in chloroform as a common solvent of both. The two polymers were mixed using a magnetic stirrer for about 4h at 60 °C to give a homogeneous solution of a blend of PMMA-PPY.

3.4. Synthesis of ZrO_2/PMMA-PPY nanocomposites

To the aforementioned solution, various amounts of 0.2(NCP1), 0.4(NCP2), 0.6(NCP3), 0.8(NCP4) and 1.0 (NCP5) wt% of ZrO_2 were added and stirred for about ½ hour at room temperature. The final solution ZrO_2/PMMA-PPY was cast in Petri dishes and kept drying at 80°C in a vacuum to obtain the nanocomposite.

4. RESULTS AND DISCUSSION

4.1 . FTIR studies

The FT-IR spectra of B(PM-PP) &B(PM-PP)ZNCP are shown in Figure 4.1(a-f). PMMA's FTIR spectra show that the addition of metal oxide, changes the C-O-C stretching at 1192 cm^{-1} to 1195 cm^{-1} and the C=O stretching at 1725 cm^{-1} to 1728 cm^{-1} additionally. It is possible to assign the bands seen on PMMA's FTIR spectra at around 1475 cm^{-1}, 1379 cm^{-1}, 1268 cm^{-1}, and 1146 cm^{-1} to CH_2 bond, CH_3 bonded, C-O stretching, and C-O-C stretching of B(PM-PP) .These bands are changed (1728 cm^{-1}, 1458 cm^{-1}, 1381 cm^{-1}, 1272 cm^{-1}, and 1165 cm^{-1}) by the addition of metal oxide. In B(PM-PP), C-H bonds and C-N stretching were in change of the vibrational peaks that were assigned intensities of 1061 cm^{-1} and 1196 cm^{-1} shift to 1064 cm^{-1} and 1195 cm^{-1} respectively, in PPY [18]. The zirconyl bond (Zr=O) may be responsible for the intense vibration observed at about 1118 cm^{-1}.[19] Zr-O stretching modes contain absorption bands of 455 cm^{-1} and 740 cm^{-1} [20]. Carbon dioxide adsorbed onto ZrO_2 at 840 cm^{-1} is most likely the source of C–O.[21] FTIR confirmed the presence of B(PM- PP) functional groups, with shifts in band positions indicating interaction with ZrO_2.

International Journal of Environmental Sciences
ISSN: 2229-7359
Vol. 11 No. 18s, 2025
https://theaspd.com/index.php

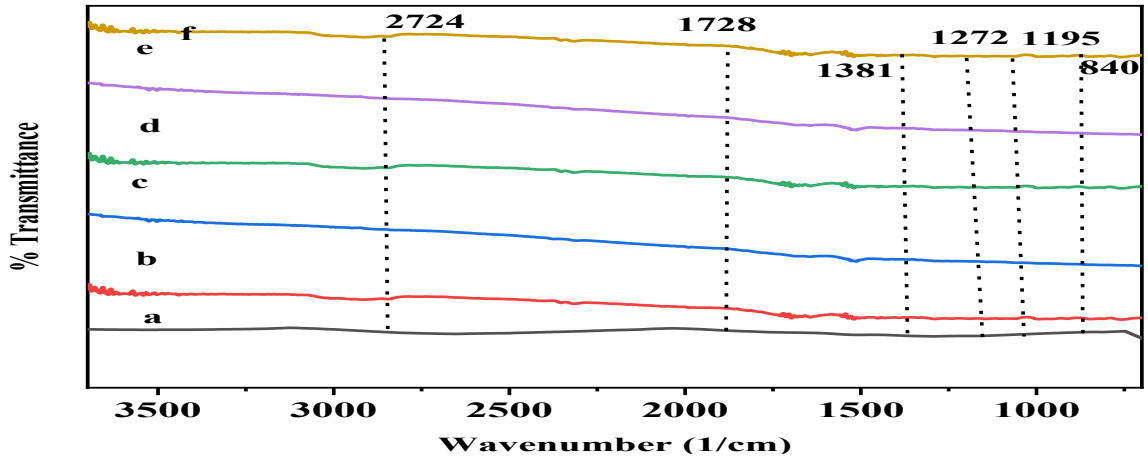

Fig.4.1. FT-IR spectra of B(PM-PP) and B(PM-PP)ZNCPs (a-B(PM-PP) b-B(PM-PP)ZNCP1,c-B(PM-PP)ZNCP2, d-B(PM-PP)ZNCP3, e-B(PM-PP)ZNCP4, f-B(PM-PP)ZNCP5)

4.2. UV-Vis studies

UV-Vis absorption spectra of B(PM-PP) and different concentrations of ZrO_2 doped with B(PM-PP) are displayed in Fig. 4.2(a-f). PMMA-PPY shows 255nm, which originates from C=O is observed in FTIR at about 1728 cm^{-1} is also appears in B(PM-PP)ZrO_2 and 315 nm π-π^* conjugation [22] shifts to 345 nm [23] addition of ZrO_2 doped with B(PM-PP). While absorbance increases with ZrO_2 concentration (0.2–1 g), adsorption also increases. Interestingly, 1g of ZrO_2 nanocomposite absorbance intensity is greater than other nanocomposite. It proved to enhance the highest current density in CV studies.

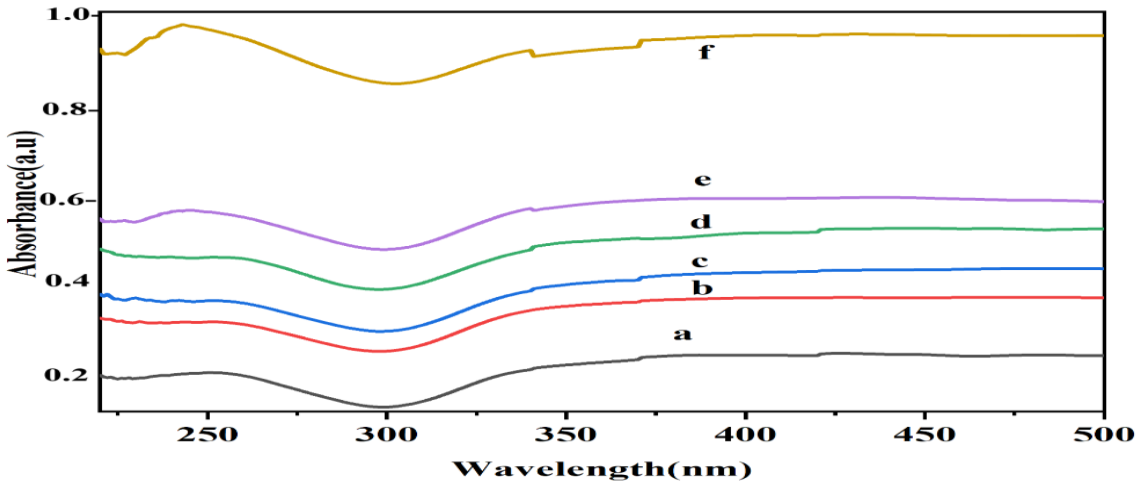

Fig.4.2 UV–Vis spectra of B(PM-PP) and B(PM-PP)ZNCPs (a-B(PM-PP),b-B(PM-PP)ZNCP1,c-B(PM-PP)ZNCP2, d-B(PM-PP)ZNCP3, e-B(PM-PP)ZNCP4, f-B(PM-PP)ZNCP5)

4.3. Band gap

The Tauc plots produced by determining the optical energy gap by converting UV–Visible spectra are shown in Fig. 4.3 (a–f). The band gap value 2.75eV is greater for the PMMA&PPY polymer blend than the value reported in the literature [22]. The band gap values are shown in Table 1.The below conclusions are consistent with the results of the literature [23] this is in agreement with the relation between the band gap energy and the lattice defects, which implies that the larger band gap energy results in a small lattice constant. lattice causes the bottom of the conduction band to move toward lower energies, while the top of the valence band remains unchanged and the band gap gradually narrows. These defects might be caused by localized states in the band gap when ZrO_2 nanocomposites interact with B(PM-PP) chains. The band gap value is slightly greater when compared to the value found in the literature [24,25] and the B(PM-PP) band gap value (2.75eV). UV-Vis analysis revealed that higher ZrO_2 content enhanced conjugation and decreased optical bandgap.

International Journal of Environmental Sciences
ISSN: 2229-7359
Vol. 11 No. 18s, 2025
https://theaspd.com/index.php

Fig.4.3 Tauc plot of B(PM-PP) and B(PM-PP)ZNCPs

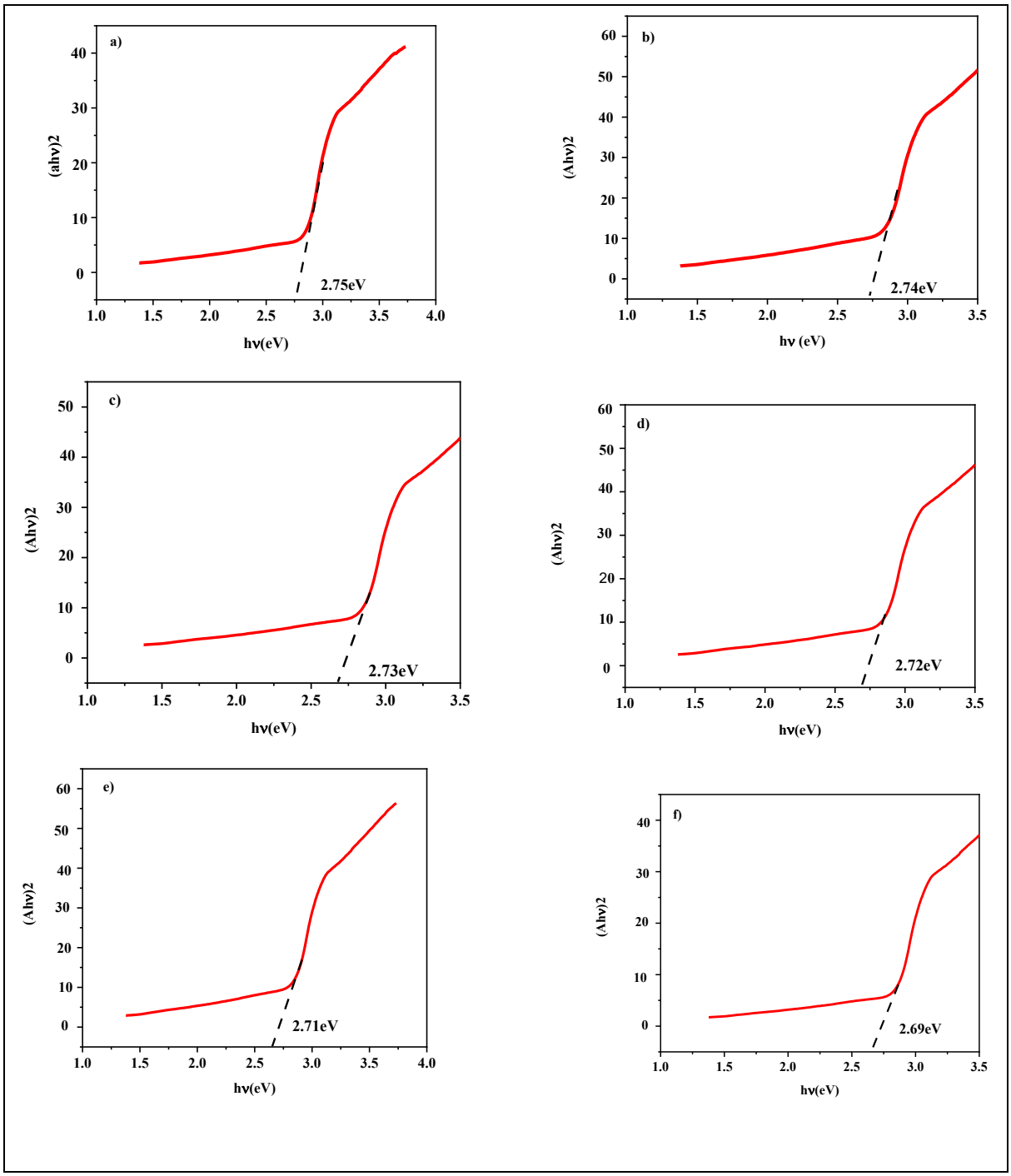

(a-B(PM-PP), b-B(PM-PP)ZNCP1,c-B(PM-PP)ZNCP2, d-B(PM-PP)ZNCP3, e-B(PM-PP)ZNCP4, f-B(PM-PP)ZNCP5)

4.4.XRD studies

The crystal's size, strain, dislocation, and structure may all be examined using X-ray powder diffraction patterns.The XRD pattern of polymer blend and nanocomposites appears in Fig. 4.4(a-f). The B(PM-PP) XRD pattern appears amorphous nature. The various B(PM-PP)ZNCP peaks, located at about (2θ) = 30.63°, 50.51°, and 60.48°, respectively, correspond to the (1 1 1) (2 0 2) and (3 1 1) planes [26]. The reference XRD pattern (JCPDS file no.:96-152-1754) matches and validates these values of ZrO_2.The average crystallite size increases in parallel with the ZrO_2 concentration, as shown in Table 1. It also suggests that as the dislocation density decreases, strain values change and electrical conductivity increases.

Conductivity increases because 1g has the lowest dislocation density. XRD confirmed the incorporation of crystalline ZrO_2 phases.

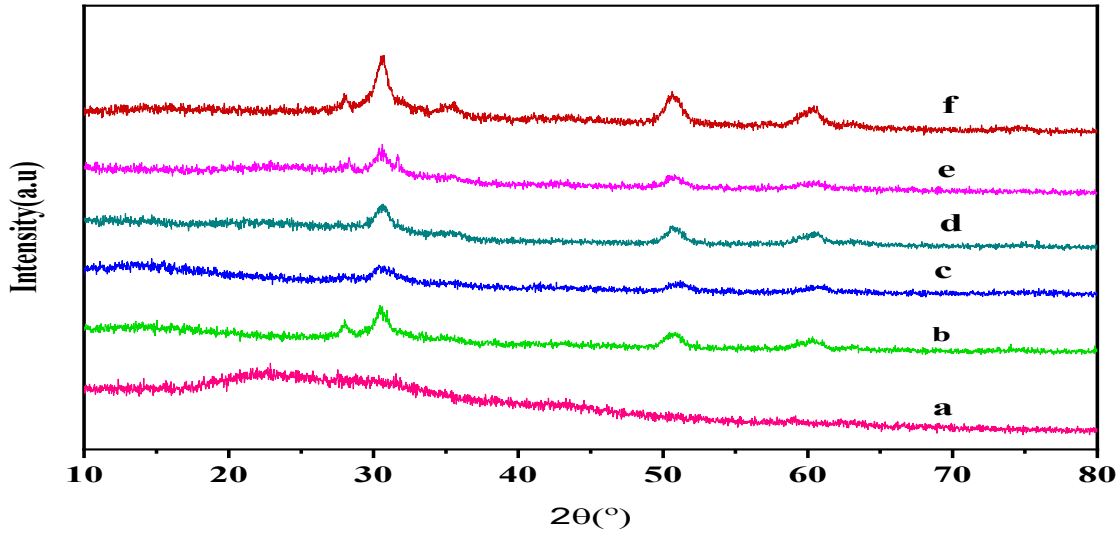

Fig.4.4. XRD pattern of B(PM-PP) and B(PM-PP)ZNCPs (a-B(PM-PP) b-B(PM-PP)ZNCP1,c-B(PM-PP)ZNCP2, d-B(PM-PP)ZNCP3, e-B(PM-PP)ZNCP4, f-B(PM-PP)ZNCP5)

Sample	Bandgap(eV)	Crystalline size 'd' [nm]	Dislocation density$\delta\times10^{18}[m^{-2}]$	Strain(ε)$\times10^{-3}$
B(PM-PP)ZNCP1	2.74	13	0.007371	0.008355
B(PM-PP)ZNCP2	2.73	14	0.007143	0.008367
B(PM-PP)ZNCP3	2.72	22	0.002028	0.006194
B(PM-PP)ZNCP4	2.71	26	0.004567	0.006548
B(PM-PP)ZNCP5	2.69	41	0.000517	0.005559

Table 1.Band gap value, Crystalline size, Dislocation density, strain of B(PM-PP)ZNCP(1-5)

4.5. TGA studies

For the TGA and HRTEM tests, I have chosen 1g of ZrO_2 nanocomposite because it showed a small band gap, excellent crystallinity, low dislocation density, and was confirmed by Catalytic performance using CV studies.

For B(PM-PP)& B(PM-PP)ZNCP5 the TGA curves are shown in Fig. 4.5(a,b) Weight loss stages were shown to exhibit three distinct phases throughout the temperature range of 40° to 970°C B(PM-PP) shift to 31° and 930°C B(PM-PP)ZNCP5.

The first weight loss moves B(PM-PP) to B(PM-PP)ZNCP5, the nearly 27°C and 8% due to the evaporation of intra- and intermolecular moisture [27]. The second weight loss stages quite gradually decrease, and the remaining mass was polymer blend to nanocomposite at 20°C and 24.5% [28]. The thermal breakdown of the polymer blend backbone, which occurred in the third stage of thermal degradation temperatures higher than 450–970°C and (38.6%), was partially responsible for this weight loss of B(PM-PP). The breakdown of PPy and the other additional third stages of weight loss, which take place between 430 and 500° C and (99.4%), are indications of mass loss and the disintegration of low molecular weight polymers and oligomers of B(PM-PP)ZNCP5. The fourth step of thermal degradation caused the backbone of the polymer blend to thermally break down above 930 °C and (123.7%), exceeding the value reported in the literature [26]. Thermal analysis via TGA showed better thermal stability with increased ZrO_2.

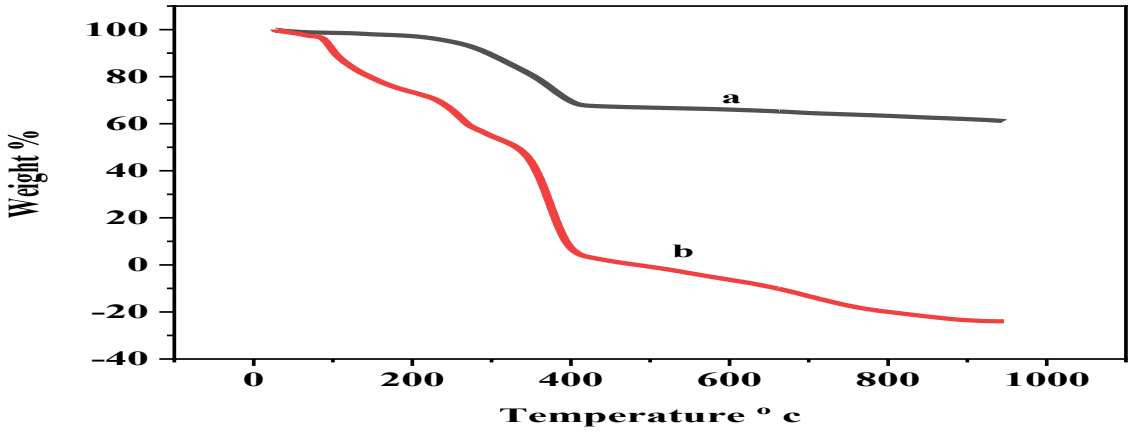

Fig. 4.5. TGA curves of a)B(PM-PP) b)B(PM-PP)ZNCP5

4.6. HR-TEM studies

The HR-TEM micrographs and SAED patterns analysis of B (PM-PP) &B(PM-PP)ZNCP5 are shown in Fig. 4.6(a-d) &4.7(a-d). The PMMA's transparent circular layer most likely embeds the PPY in the darker rectangle area shown in Fig. 4 .6a and b. The SAED pattern of B(PM-PP) in Fig. 4.6c shows a cluster of diffraction spots, which is confirmed by the amorphous peak structure in XRD.A standard deviation of 1.19 nm and an average particle size of 97 nm will be predicted for B(PM-PP).

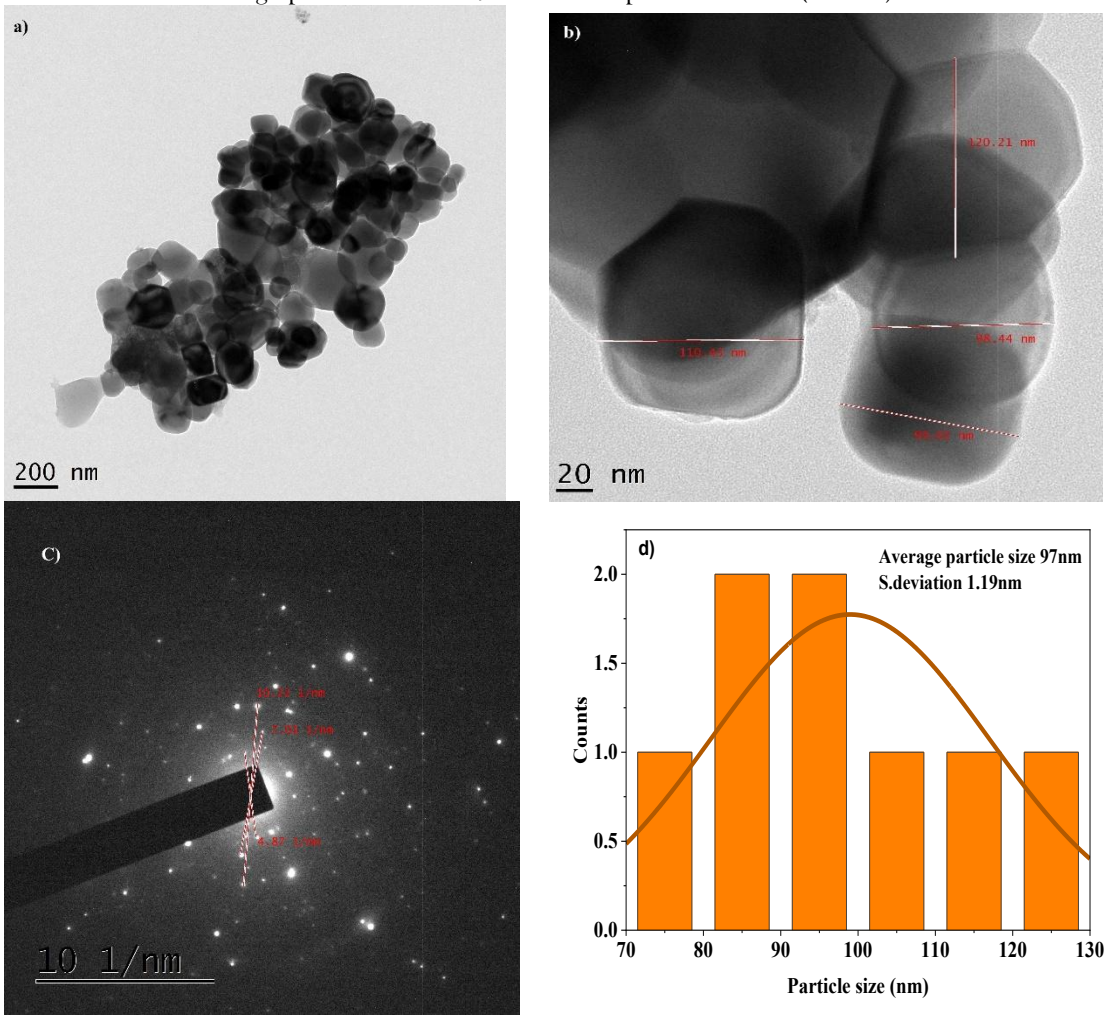

Fig. 4.6. a,b HRTEM with different scales of magnification; c SAED pattern; d and particle size distribution histogram of B(PM-PP)

A circular PMMA shape is placed between PPY and around the rectangular dark strands, and a component surface gets embedded in each ZrO_2. Fig. 4.7a shows the volume loaded by the B(PM-PP)ZNCP5 matrix shows a porosity.In addition to revealing details on the lattice fringes of these nanoparticles, the SAED patterns under the XRD data demonstrate that the B(PM-PP)ZNCP5 is polycrystalline. Fig. 4.7c. The lattice planes of (1 1 1), (2 0 0), (2 0 2), (2 2 2), and (4 0 0) are represented by the corresponding fringes of (d=3.26,2.49,1.73,1.43, and 1.23). Because the polycrystal of ZrO_2 nanoparticles are composed of several homogeneous layers, associated SAED pattern. As indicated by Fig. 4.7d, the log-normal distribution function is typically used to match the particle size distribution histogram of the nanocomposite. An average particle size of 13.5 nm with a standard deviation of 1.37 nm as seen (eqn.1) is predicted for nanocomposites. HRTEM imaging demonstrated even nanoparticle dispersion at optimal concentrations.

$$f(D) = (1/\sqrt{2\pi}\,\sigma D)\exp[-\ln^2(D/D_0)/2\sigma^2] \quad \text{---------(1)}$$

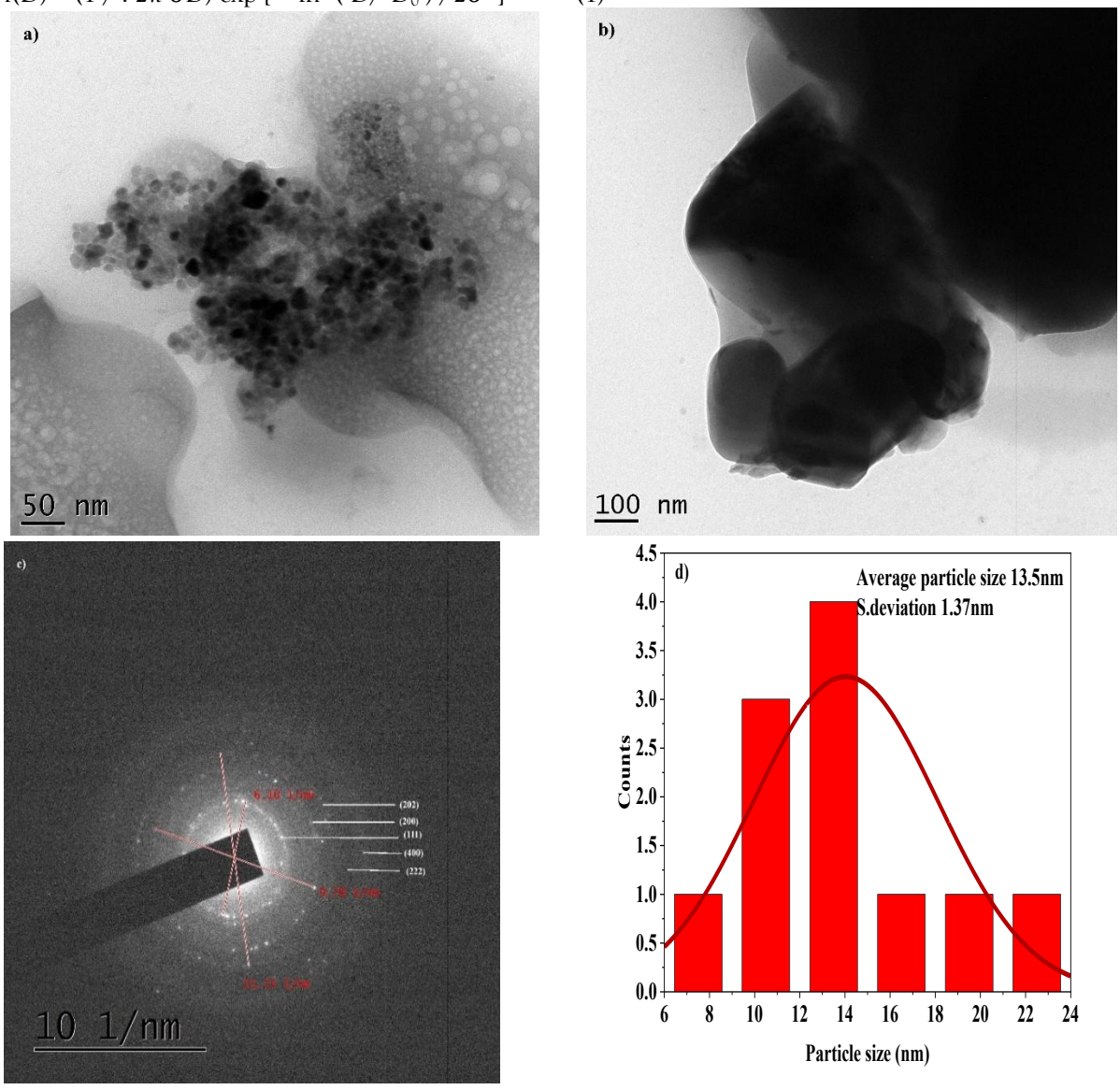

Fig. 4.7. a,b HRTEM with different scales of magnification; c SAED pattern; d and particle size distribution histogram of B(PM-PP)ZNCP5

4.7. Electrochemical characterization

Under several atmospheric (N_2 and O_2) gas conditions, pH, and concentration variations, the B(PM-PP), B(PM-PP)ZNCP1-B(PM-PP)ZNCP5 modified GCE was examined by cyclic voltammetric analysis using scan rates between 50 to 500 mV/s and -1.0 to 1.4 V.

4.7.1. Effect of pH

As shown in Fig. 4.8(a,b) the effect of pH on the voltammetric response was therefore investigated at the B(PM-PP) & B(PM-PP)ZNCP5 modified GCE in the pH range of 1.0 to 13.0 using pH buffer solutions that had been adjusted to the required condition. The studies that follow utilize pH 1.0 since it appears to be the optimal range for a sensitive response.

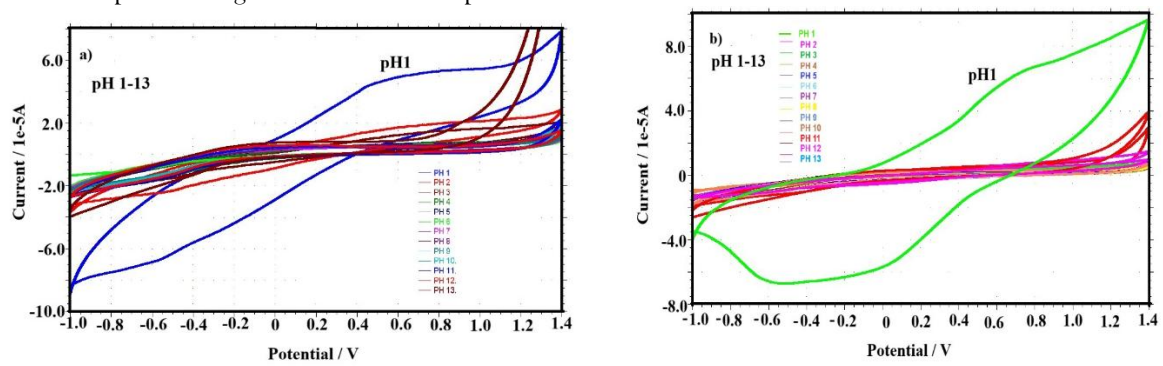

Fig. 4.8 Cyclic voltammetric responses obtained with different pH 1-13 of 50 mV/s for a)B(PM-PP)-modified GCE b) B(PM-PP)ZNCP5-modified GCE

4.7.2. Effect of concentration:

The effect of concentration of ZrO_2 were carried out by cyclic voltammetry methods. As the quantity of ZrO_2 increased, current density also increased (Fig. 4.9). The lowest onset potential and highest current density appear with a 1g ZrO_2 dopped with polymer blend. Since B(PM-PP)ZNCP5 shows a higher current peak at a lower potential than B(PM-PP)ZNCP1-B(PM-PP)ZNCP4 and B(PM-PP), it is selected for further electrochemical investigation. TGA, HR-TEM, and XRD experiments provide additional support for the optimization of this nanocomposite.

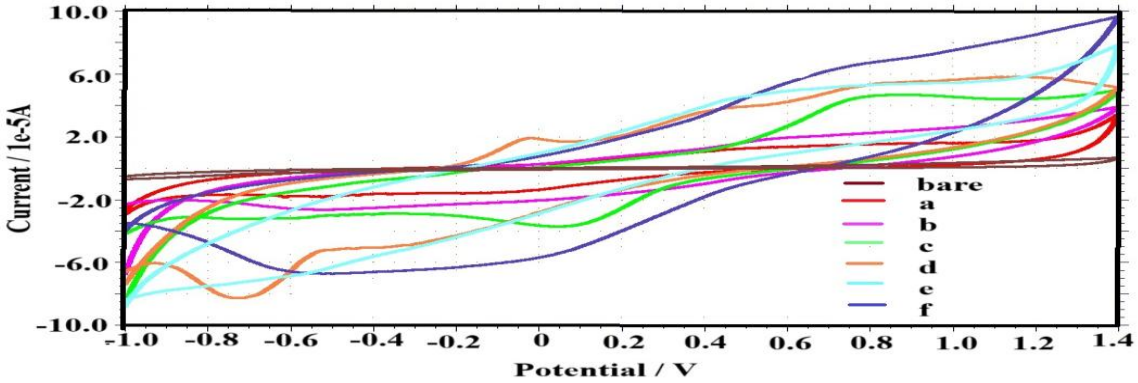

Fig.4.9. Cyclic voltammetric responses obtained with a scan rate of 50 mV/s for B(PM-PP)ZNCP-modified GCE (a-B(PM-PP),b-B(PM-PP)ZNCP1, c-B(PM-PP)ZNCP2, d-B(PM-PP)ZNCP3, e-B(PM-PP)ZNCP4,f-B(PM-PP)ZNCP5)

4.7.3. Effect of atmosphere:

The cyclic voltammogram shows defined oxidation–reduction (redox) peaks determined at 50 mV/s. The voltammograms for the B(PM-PP)/GCE &B(PM-PP)ZNCP5/GCE in pH1 were carried out in normal as well as O_2 and N_2-saturated buffer, shown in (Fig.4 .10a & 4.10 b). The results demonstrate that B(PM-PP)&B(PM-PP)ZNCP5 have improved in O_2-saturated buffer.

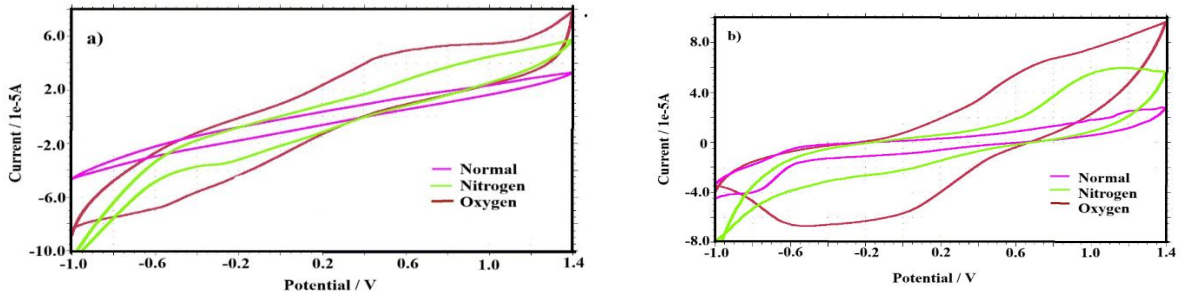

Fig.4.10.a,b). Cyclic voltammetric responses obtained with a scan rate of 50mV/s for B(PM-PP) and B(PM-PP)ZNCP5 modified GCE

4.7.4. Effect of scan rate:

At 50-500 mV/s, the B(PM-PP)& B(PM-PP)ZNCP5-modified GCE's equally well-defined CV (Fig. 4.11a&4.12a) demonstrates that it is electroactive. The plot of current vs square root of scan rate (Fig.4.11b and 12b) shows that the anodic current develops quite linearly in accordance with the equation y=0.00388+0.06396; R^2=0.99844(for B(PM-PP)) and y=0.00498x+0.08216; R^2=0.99884 (for B(PM-PP)ZNCP5), The experimental slope value is known to be lower than the theoretical value of 0.5, which suggests that the process is diffusion controlled.[29] Diffusion coefficients for B(PM-PP) films were determined to be 6.584×10^{-6} cm^2 /s and B(PM-PP)ZNCP5 films were 2.942×10^{-5} cm^2 /s as caluculated in (eqn.2). The diffusion coefficient indicates that effective charge transfer activities are made possible by the electroactive species' ability to diffuse quickly across the electrolyte solution.The increased electrocatalytic activity of B(PM-PP)ZNCP5 in the nanocomposite resulted in a higher diffusion coefficient than the polymer blend.

The Randles-Sevcik technique (eqn. 2) is used to calculate the peak current from the Nernstian or reversible systems, as shown below:

$$Ip = 2.69 \times 10^5 \, n^{3/2} A D^{1/2} C \vartheta^{1/2} \quad \text{.....(2)}$$

Ip stands for the peak current, A for the electrode area (0.071 cm^2), n for the number of transferred electrons in the redox reaction (1), C for the concentration (1 M), D for the diffusion coefficient of the transferred species, and S for the scan rate (100 mV/s).

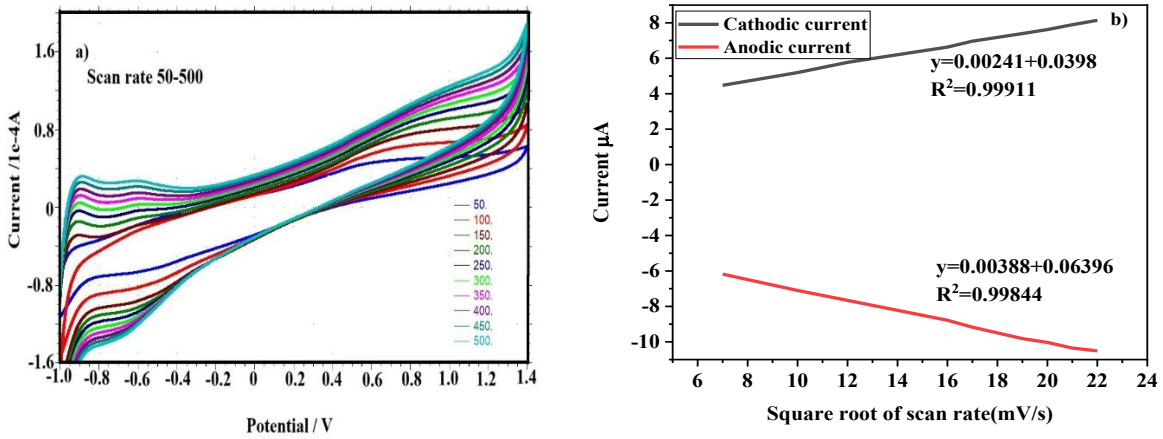

Fig.4.11. a,b)Cyclic voltammetric responses obtained with a scan rate of 50-500 mV/s for B(PM-PP) modified GCE

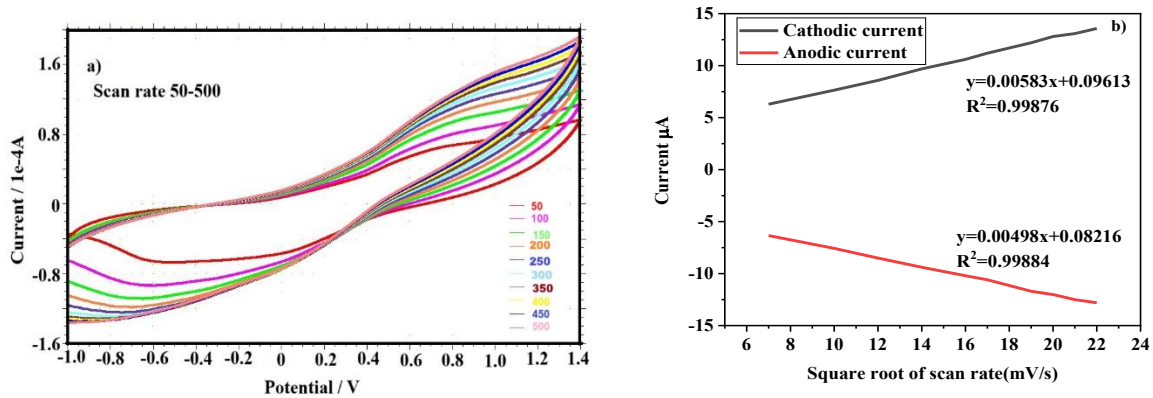

Fig.4.12.a,b). Cyclic voltammetric responses obtained with a scan rate of 50-500 mV/s for B(PM-PP)ZNCP5 modified GCE

4.7.5. Chronoamperometry Studies

In a modified GCE, B(PM-PP)and B(PM-PP)ZNCP5 the two-phase potential-step chronoamperometric study was performed using buffer solutions of normal, N_2, and O_2 saturated buffers shown in Fig. 4.13 (a,b). A high current was observed for O_2 saturated buffer, which is however less in the case of the normal

and N_2-saturated buffer. Thus, the oxygen gas (O_2) interfered with the interaction between the polymer blend- metal oxide layers and enhanced the current. Based on the slope value of I vs. t-1/2 in both the O_2 and N_2 atmospheres as well as under normal circumstances, the Cottrell (eqn. 3) was used to calculate the diffusion coefficient values of B(PM-PP) & B(PM-PP)ZNCP5 modified GCEs. For the B(PM-PP)ZNCP5 modified GCE, the diffusion coefficient (D) and surface coverage (Np) values are shown in Table 2. B(PM-PP)ZNCP5's D value and Np value are greater in O_2-saturated buffer than it is in N_2 and normal saturated buffers. For the electrode in B(PM-PP)ZNCP5 in an oxygen environment, our results show stable catalytic activity. The value of the diffusion coefficient ($3.14x10^{-6}$) &Np value ($1.29x10^{-6}$) of B(PM-PP)ZNCP5 is higher under O_2 circumstances than in B(PM-PP) diffusion coefficient value ($4.1x10^{-6}$) and Np value ($1.10x10^{-7}$). The electrode material's strong N_p and favorable D values indicate that it has both significant diffusion properties and good catalytic activity, that function in collaboration to improve its overall electrochemical performance.[30]

The Cottrell (Eq.3) was used to determine the diffusion coefficient values of B(PM-PA) modified GCE using the slope values of I vs. $t^{-1/2}$.

Slope = $nFD^{1/2} ACp\pi^{-1/2}$ ------(3)

Here, D (cm^2 s^{-1}) is the diffusion coefficient of B(PM-PA) in pH1, Cp (mol cm^{-3}) is the concentration of the electroactive B(PM-PA) in pH1, and A (cm^2) is the geometric area of the GC electrode. Using the formula Cp = Np / Al, which takes account of both the film thickness (l) and the amount of electroactive species (Np) present on the surface of the B(PM-PA) modified electrode, can determine the concentration of electroactive species (Cp). Np = Q / nFA, where Q is the charge consumed, n is the number of electrons involved in the catalyst's reduction, and F is the Faraday constant (96485 C mol^{-1}), was used to calculate the surface coverage of the electroactive species from cyclic voltammograms at low scan rates (50 mVs^{-1}). The slope values are taken from the chronoamperometric curves.

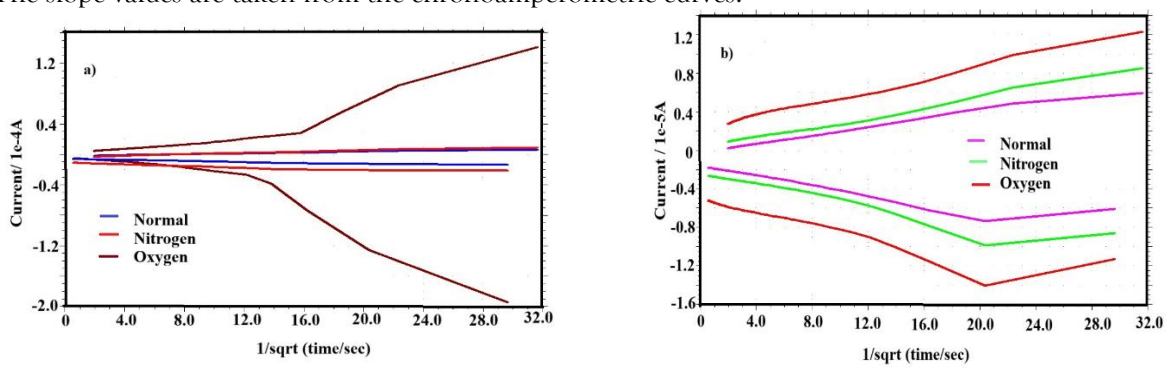

Fig.4.13. Chronoamperogram of a) B(PM-PP)/GCE b) B(PM-PP)ZNCP5 /GCE at pH1

4.7.6. Chronocoulometry studies

Using a Double potential step technique, B(PM-PP) and B(PM-PP)ZNCP5 modified the chromatocoulometric behavior of GCE and was examined with and without N_2 and O_2 saturated buffer. A B(PM-PP)ZNCP5 modified GCE chronocoulomogram Fig.4.14 (a,b) shows that the O_2 saturated buffer is much more charged than the N_2 saturated buffer and normal. CC confirmed that the charge consumption is more efficient in the presence of oxygen.

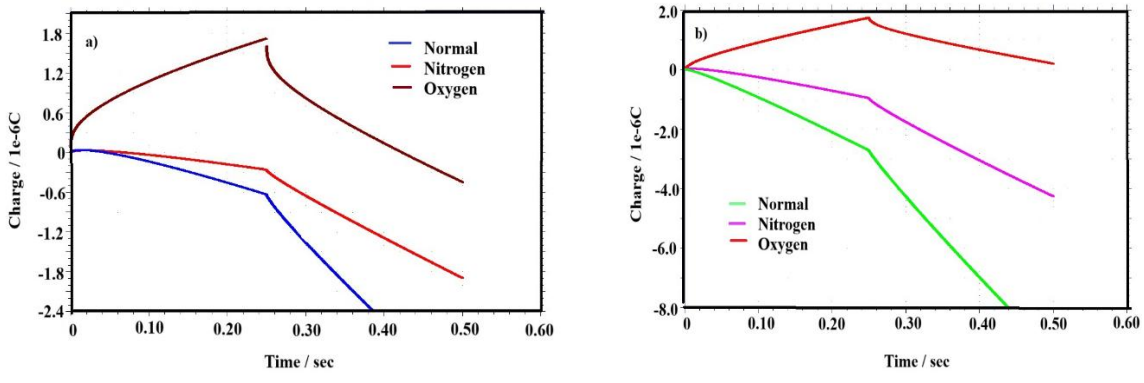

Fig. 4.14. Chronocoulomogram responses obtained for a)B(PM-PP)/ GCE b) B(PM-PP)ZNCP5 at pH1

4.7.7. Impedance spectroscopy

Electrochemical impedance across a frequency range of 1000 to 0.01 Hz was assessed using the open circuit potential. The resistance specific to fuel cells is determined using the electrochemical impedance spectra Nyquist plots, Z' vs. Z", acquired via EIS analysis. Fig. 4.15 (a,b) displays B(PM-PP) &B(PM-PP)ZNCP5 at pH 1. The double-layer capacitance is calculated from Eqn. 4 and Rs and Rct values are derived from Nyquist plot. Different atmospheric circumstances affect Rct and Cdl values, as shown in Table 2. In an oxygen environment, the electrode of B(PM-PP) and B(PM-PP)ZNCP5 showed the Rct values are 66.6Ω, 56.8Ω, and Rs values are 25.0KΩ and 13.0KΩ, respectively, suggesting a notable decrease in electron-transfer resistance and an increase in the rate of reaction.[31] This finding is explained by the fact that the electrocatalytic activity of B(PM-PP)ZNCP5 is somewhat greater than the B(PM-PP). Impedance data supported these findings, with a decrease in charge transfer resistance in the oxygen environment.

$$Cdl = 1/ 2\pi FmaxRct \text{ .....(4)}$$

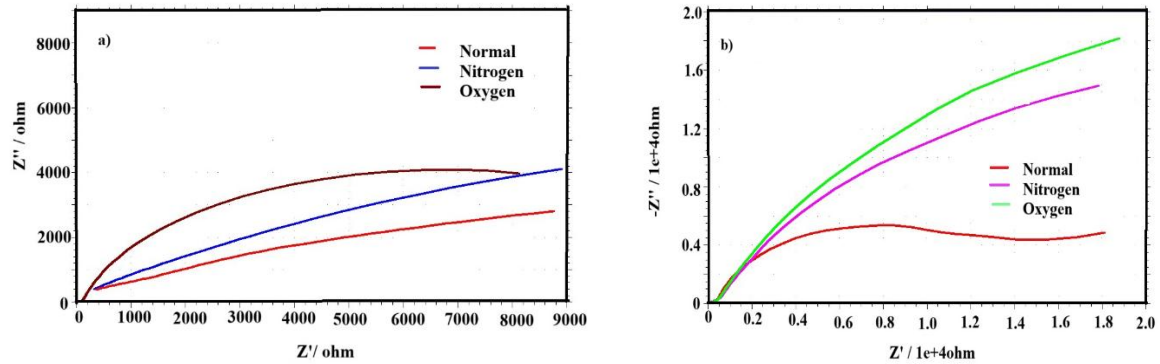

Fig.4.15. Impedance responses obtained for a)B(PM-PP)/GCE b)B(PM-PP)ZNCP5/GCE at pH1

Sample	atmosphere	Np	Diffusion coefficient	Bulk resistance R_s(KΩ)	Charge transfer resistance R_{ct}(Ω)	Double layer capacitance C_{dl} (Fcm^{-2})
B(PM-PP)	Normal	$6.03x10^{-8}$	$6.025x10^{-7}$	63	72.4	$2.55x10^{-7}$
	Nitrogen	$3.44x10^{-8}$	$3.438x10^{-7}$	42	74.5	$1.48x10^{-7}$
	Oxygen	$1.10x10^{-7}$	$4.1000x10^{-6}$	25	66.6	$1.36x10^{-7}$
B(PM-PP)ZNCP5	Normal	$6.31x10^{-7}$	$1.58x10^{-7}$	73	59.0	$2.696x10^{-7}$
	Nitrogen	$9.90x10^{-7}$	$9.67x10^{-6}$	37	57.2	$6.499x10^{-6}$
	Oxygen	$1.29x10^{-6}$	$3.14x10^{-6}$	13	56.8	$5.573x10^{-6}$

Table 2. Np and Diffusion coefficient and Impedence Parameters Values responses obtained for B(PM-PP) & B(PM-PP)ZNCP5 modified GCE at different atmosphere.

4.7.8. Linear Sweep Voltammetric Studies

In LSV, the B(PM-PP) and B(PM-PP)ZNCP5 modified GCE was carried out using normal, O_2, and N_2 saturated buffers are shown in Fig. 4.16 (a,b), at pH1. Table 3 shows a notable range of electrocatalytic activity is observed in an oxygen atmosphere

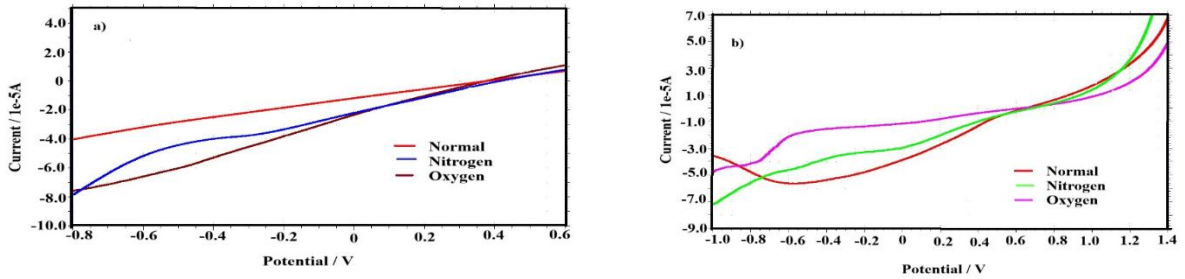

Fig.4.16. Linear Sweep Voltammetric cathodic peak responses with a scan rate of 50 mV/s for a)B(PM-PP) modified GCE b)B(PM-PP)ZNCP5 modified GCE

4.7.9. Effect of p-nitrophenol at Atmospheric Conditions in Linear Sweep Voltammetric Studies

In LSV, the B(PM-PP) & B(PM-PP)ZNCP5 modified GCE were carried out at 50 mV/s using normal, O_2, and N_2 saturated buffers in acidic p-nitrophenol (equal molar solution of H_2SO_4&p-nitrophenol) Fig. 17 (a,b). As shown in Table 3, the cathodic peak current (-945.0mV) in the B(PM-PP)ZNCP5 modified GCE is much greater (220mV) than in cathodic current (-725.5mV) in B(PM-PP). The potential moves to the negative side nearly 1000mV in an O_2-saturated buffer. Thus, the p-nitrophenol reduction peak value shows higher in the linear sweep voltammogram at 50 mV/s. Because of its nitro groups and aromatic rings, p-nitrophenol reduces more quickly and efficiently by interacting strongly with conducting polymers' conjugated π-electron systems, and additionally, p-nitrophenol molecules can be adsorbed by the many hydroxyl groups on the surface of ZrO_2.[32, 33]

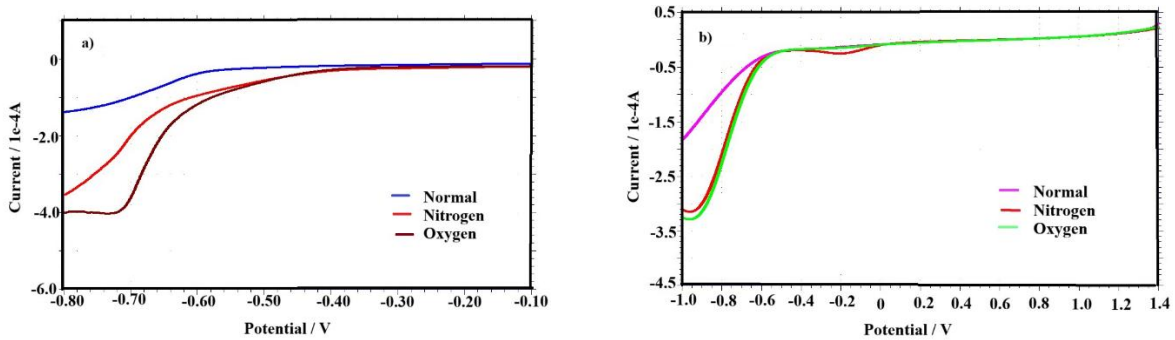

Fig.4.17. Linear Sweep Voltammetric cathodic peak responses obtained for a)B(PM-PP) b) B(PM-PP)ZNCP5 presence of acidic P-nitrophenol.

Sample		Normal	Nitrogen	Oxygen
B(PM-PP)	~~~	broad	broad	-319.2mV
	N-Phenol reduction	-634.0mV	-643.7mV	-725.5mV
B(PM-PP)ZNCP5	~~~	broad	-480.6mV	-753.6mV
	N-phenol reduction	broad	-942.4mv	-945.0mV

Table 3. Reduction parameters were obtained by B(PM-PP)and B(PM-PP)ZNCP5 modified GCE at different atmosphere

4.7.10.Proposed mechanism for B(PM-PP) & B(PM-PP)ZNCP5 reduction of P-nitrophenol

The reduction of PNP involves a two-electron process, leading to the formation of para-aminophenol. The conducting matrix of PMMA-PPY provides a supportive redox-active environment. The presence of ZrO_2 facilitates this by increasing oxygen adsorption sites and assisting charge mobility. A radical that disrupts B(PM-PP)& B(PM-PP)ZNCP5 may form as a result of interactions between the nitro group. The mechanism of the reaction is shown in eqn. 5&6. It was found that the cathodic peak's irreversible potential was -725.5 mV of B(PM-PP) and -945.0mV of B(PM-PP)ZNCP5. Typically ~0.40 - 0.70mV Vs AgCl (2e⁻nitroso intermediate), ~0.70-0.90mV Vs Ag/AgCl (2e⁻to hydroxylamine) and ~ 0.9-1.1mV vs AgCl (2e⁻to amine) [34].It is possible to reduction of P-nitrophenol depending upon potential using this approach on the B(PM-PP) &B(PM-PP)ZNCP5 modified electrode as shown in scheme 1.

$B(PM\text{-}PP)\text{-}NO + 2H^+ + 2e^- \rightarrow B(PM\text{-}PP)\text{-}NHOH$ .....(5)

$B(PM\text{-}PP)ZNCP5\text{-}NHOH + 2H^+ + 2e^- \rightarrow B(PM\text{-}PP)ZNCP5\text{-}NH_2 + H_2O$ .....(6)

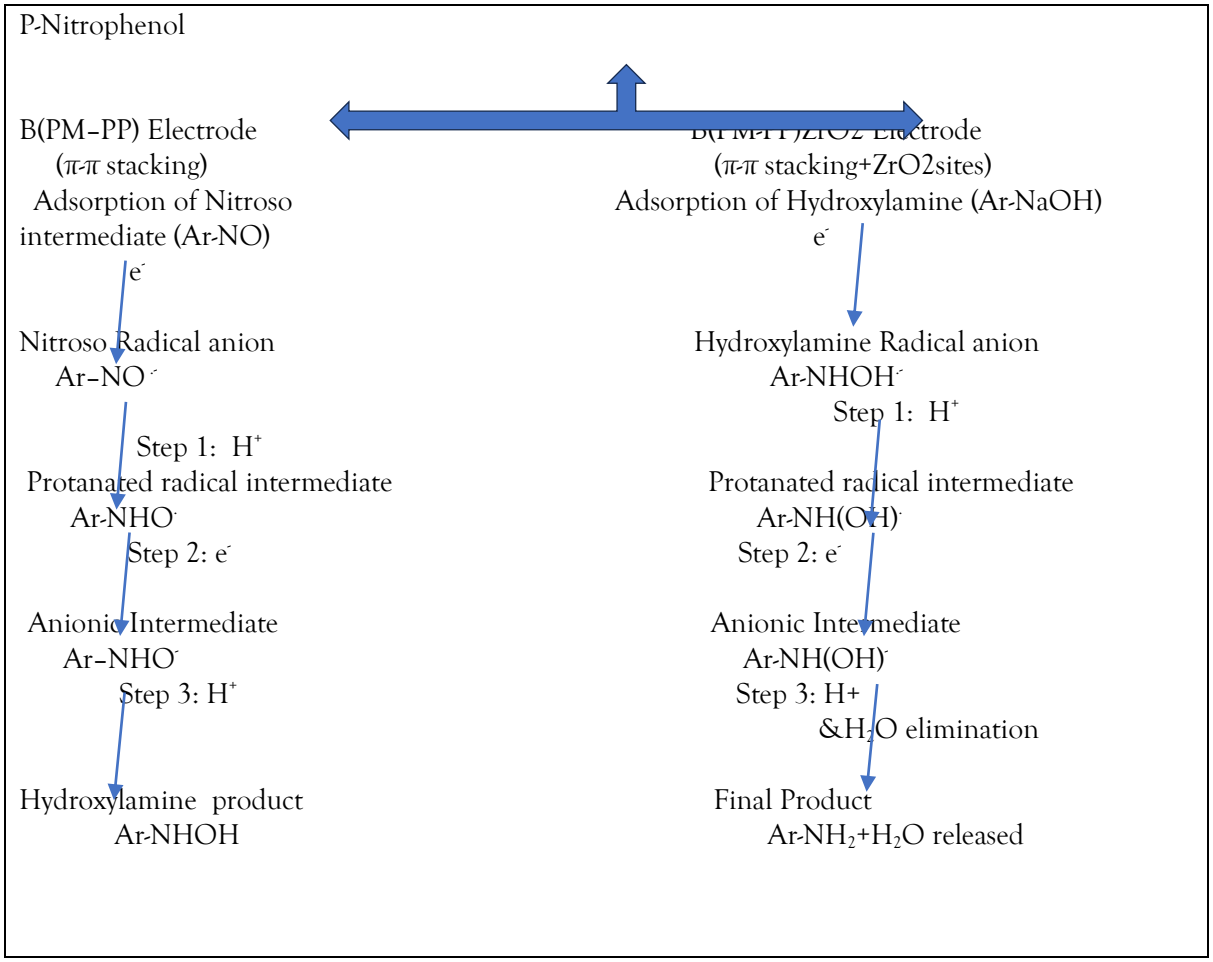

Scheme 1: Schematic representation of the Mechanism of p-Nitrophenol reduction on B(PM-PP)&B(PM-PP)ZNCP5.

5. CONCLUSION

We successfully synthesized the environmentally friendly B(PM-PP)ZNCP5 and used it for reduction applications. The poly-crystalline structure of the nanocomposite was discovered by X-ray diffraction (XRD) structural investigations, and the high average crystallite size of B(PM-PP)ZNCP5 was 41 nm. To demonstrate the porosity of the material, the proportion of B(PM-PP)ZNCP5 embedded in the nanocomposite can also be observed on HRTEM at an average particle size of 13.5 nm. TGA proved that B(PM-PP)ZNCP5 was thermally stable at 930°C. In terms of ZrO_2 weight %, the CV curves show that the current increase by these catalysts increases from 0.2g to 1g. According to chronoamperometry and chronocoulometry, the B(PM-PP)ZNCP5 modified GCE shows a high current under O_2 than normal and in N_2-saturated solution at pH 1.0. An analysis of B(PM-PP)ZNCP5 modified GCE states revealed that electrocatalytic activity increased in acidic p-nitrophenol solution in oxygen atmosphere. This investigation demonstrates the importance of B(PM-PP)ZNCP5 nanocomposite in an oxygen atmosphere in designing effective PNP reduction. This B(PM-PP)ZNCP5 environmentally benign synthesis and responsive behavior under various gas conditions suggest strong potential for real-world environmental reduction technologies.

Acknowledgements

The authors appreciate the support provided by their respective institutions and research facilities.

Environmental Relevance Statement

This research contributes to the development of green and responsive sensors for toxic pollutant monitoring. By tailoring material design and sensing atmosphere, the study promotes sustainable reduction methods for real-time environmental safety.

REFERENCES

1. Zhifeng, J, Jimin, X, Deli, J, Xiaojun, W& Min, C 2013, 'Modifiers-assisted formation of nickel nanoparticles and their catalytic application to p-nitrophenol reduction', Crystal Engineering Communications, vol. 15, no.3, pp.560-569.

2. Zhifeng, J, Jimin, X, Deli, J, Xiaojun, W & Min, C 2013, 'Modifiers-assisted formation of nickel nanoparticles and their catalytic application to p-nitrophenol reduction', Crystal Engineering Communications, vol.15, no.3, pp.560-569.

3. Alan Omar, CJ, Edgar Ivan, OL, Mohan, KK& Naveen Kumar, RB 2024, 'Advances in 4-Nitrophenol Detection and Reduction Methods and Mechanisms: An Updated Review', ACS Omega, vol. 9, no. 31, pp. 33335–33350.

4. Benzhi L, Tian W, Chuntao Y & Zhenglong W 2014, 'Electrochemical analysis of p-nitrophenol in acidic or alkaline medium using silver nanoparticle decorated multi-walled carbon nanotubes', Journal of Materials Science, vol.49, no.15, pp.5398–5405.

5. Madhushree, R, Jadan Resnik Jaleel, UC, Dephan, P & Sunaja Devi, KR 2022, 'The catalytic reduction of 4-nitrophenol using MoS2/ZnO nanocomposite', Applied Surface Science Advances, vol.10, no.1, pp.100265-100274.

6. Maolin, L & Guofang, C 2013, 'Revisiting catalytic model reaction p-nitrophenol/$NaBH_4$ using metallic nanoparticles coated on polymeric spheres', Nanoscale, vol.5, no.1, pp. 11919-11927.

7. Libo, S, Yin, Z, Jie, Z, Xinyuan, R, Zhang, M, Song, W, Xu, Z& Qi, C 2022, 'Gold nanoparticles supported on poly (aniline-co-pyrrole) as the efficient catalysts for the reduction of 4-nitrophenol', Molecular Catalysis, vol.525, no.1, pp.112362-112370.

8. Abdulwahhab, HM, Leqaa, AM, Omar, GH, Shankar, S, Mustafa, AA, Kuldeep, KS, Safaa, AD, Israa, KM, Mustafa, MJ & Ummal, NS 2022, 'A Review on Polyaniline: Synthesis, Properties, Nanocomposites, and Electrochemical Applications', International Journal of Polymer Science, vol. 2022,no.5, pp.1-20.

9. Hao, L, Dong, C & Yu, D 2024, 'Polypyrrole Derivatives: Preparation, Properties and Application', Polymers, vol. 16, no.16, pp. 2233-2239.

10. Namrata, D, Avisek, B, Debmalya, R& Priyadarsi, D 2022, 'Methyl Methacrylate-Based Copolymers: Recent Developments in the Areas of Transparent and Stretchable Active Matrices', ACS Omega, vol.7, no.42,pp.36929-36944.

11. Li, Y, Liu,B,Liu, J, Wang, T,Shen,Y Zheng, K, Jiang, F,Xu, Y& Liu, X 2021, 'Tuning the Lewis acidity of ZrO2 for efficient conversion of CH4 and CO2 into acetic acid', New Journal of Chemistry, vol.45, no.20, pp.8978-8985.

12. Yao, S, Ke, W, Lu, L, Jingkai, Z, Jiexu, Y, Ping, C, Xiang, G& Shihan, Z 2024, 'Facilitating proton-coupled electron transfer for energy-efficient CO2 desorption by C@ZrO2 hollow composites', Chemical Engineering Journal, vol.495, no.1, pp.153332-153338.

13. Shaik, MR, Syed, F, Kuniyil, M, Sharif, M, Alwarthan, A, Rafiq, M, Ali, M,Tahir, M &Khan, M 2020, ' Facile Sonochemical Preparation of Au-ZrO2 Nanocatalyst for the Catalytic Reduction of 4-Nitrophenol', Applied Sciences, vol.10, no.2, pp.1-11.

14. Shtansky, DV, Levashov, EA & Sukhorukova, IV 2015, 'Multifunctional bioactive nanostructured film', Hydroxyapatite (Hap) for Biomedical Applications, Available from: Woodhead Publishing, [27 February 2015]

15. Abel, KL, Weber, S, Poppitz, D, Titus, J, Sheppard, TL & Glaser R 2022, 'Thermally stable mesoporous tetragonal zirconia through surfactant-controlled synthesis and Si-stabilization', RSC Advances, vol.12, no.26, pp.16875-16885.

16. Mahyar, M, Ayda, K & Rouhollah, M 2023, 'Nano-ZrO2: A review on synthesis methodologies', Inorganic Chemistry Communications, vol.157, no.1,pp.111293-111302.

17. Khulaif, A, Atta, A, Majed, A, Sultan, A, Alhulw, HA, 2025, 'Impact of ZrO_2 nanoparticles on surface, thermal, and structural properties of PVA/ZrO_2 composite films for advanced flexible electronics applications', Surfaces and Interfaces, vol. 59, no. 1, pp.105964-105975.

18. Yongzhu, F& Arumugam, M 2012, 'Sulfur-Polypyrrole Composite Cathodes for Lithium-Sulfur Batteries',RSC Advances, vol.2, no.14, pp.5927-5929.

19. Elmadani, AA, Tomic, N, Radovic, I, Vuksanovic, MM, Stojanovic, D, Jancic, R & Radojevic,V 2019, 'Salt template zirconia reinforcing particles as possible reinforcement for PMMA matrix composite', Advanced Composites Letters, vol.28, no.1, pp.1–7.

20. Manish, B, Arun, B, Manish, B, Rajesh, B 2021, 'Green Synthesis of Zirconia (ZrO2) Nanoparticles using Curcuma Longa Extract and Investigation of Compressive Strength of Epoxy resin (EP)/ZrO2 Nanocomposites', Journal of Nepal Chemical Society, vol. 42, no.1, pp.45-50.

21. Sweetu, BP,Baker, N,Marques, I, Azhang, H, Mathew, T,Christos, T,Craig, F,Cortino, S & Tolou, S 2017, Transparent TiO 2 nanotubes on zirconia for biomedical applications', RSC Advances,vol.7,no.48, pp.30397-30410.

22. Smita, D& Asit KK 2019, 'Enhanced photoluminescence through Forster resonance energy transfer in Polypyrrole-PMMA blends for application in optoelectronic devices', Materials Science in Semiconductor Processing, vol.103, no.10, pp.104644-104649.

23. Dhiraj, D, Rama, D, Jyoti Prasad, B& Amrit Puzari, S 2021, 'Smart pH-Responsive Polyaniline-Coated Hollow Polymethylmethacrylate Microspheres: A Potential pH Neutralizer for Water Purification Systems', ACS Omega, vol.6, no.15, pp.10095−10105.

24. Boya PN, Sivasankar, K, Prasenjit, K, Budigi, L& Badal, KM 2022, 'Photocatalytic and Antioxidant Studies of Bioinspired ZrO2 Nanoparticles Using Agriculture Waste Durva Grass Aqueous Extracts', Journal of Hazardous Materials Advances,vol 7, no.1, pp.100112-100120.

25. Study the Structural and Optical behaviour of Conducting Polymer based nanocomposites: ZrO2 -Polypyrrole Nanocomposites, IOP Conference Series Materials Science Engineering, pp.012038-012045.

26. Rizwan, U, Mehtab, K, Rozina, K, Nadia, K, Muhammad, SK &Yaser, AB 2021, Synthesis, Characterization and Evaluation of Supercapacitive Response of Dodecylbenzenesulphonic Acid (DBSA) Doped Polypyrrole/Zirconium Dioxide Composites, Polymers, vol.13, no.22, pp. 4035-4041.

27. Dhachanamoorthi, N, Oviya, K, Sathish, S, Suresh, P, Parthibavarman, M, Jeshaa Dharshini & K,Aishwarya, M 2024, 'Effective move of Polypyrrole/TiO2 hybrid nanocomposites on removal of methylene blue dye by photocatalytic activity', Chemical Physics Impact, vol. 9, no.1, pp. 100723-100730.

28. Maria, O, Juraj, P, Jurgen, P & Frank, S 1997, 'Synthesis, Electrical Properties and Stability of Polypyrrole-Containing Conducting Polymer Composite', Polymer International, vol. 43,no.1, pp.109-116.

29. Gopu, G, Baladhandapani, M,Vedhi, C & Manisankar, P 2012, 'Determination of three analgesics in pharmaceutical and urine sample on nano poly (3, 4-ethylenedioxythiophene) modified electrode', Ionics, vol.18, no.1, pp.231–239.

30. Liu, Y, Sun, J, Song, R, Liu, X, Wang, Y, & Wang, J 2019, 'Enhanced electrocatalytic activity of nitrogen-doped graphene aerogel-supported Fe–N–C catalysts for oxygen reduction reaction', Electrochimica Acta, vol.311, no.1, pp. 331–339.

31. Gul, H, Shah, A, Krewer, U & Bilal, S 2020, 'Study on Direct Synthesis of Energy Efficient Multifunctional Polyaniline–Graphene Oxide Nanocomposite and Its Application in Aqueous Symmetric Supercapacitor Devices',Nanomaterials, vol.10, no.1, pp.118-129.

32. Ghosh, AU, Koushik, AU, Sanjoy, S & Giri, PK 2024, 'Fast Reduction of 4-Nitrophenol and Photoelectrochemical Hydrogen Production by Self-Reduced Bi/Ti3C2Tx/Bi2S3 Nanocomposite: A Combined Experimental and Theoretical Study', ACS Applied Materials Interfaces, vol. 16, no. 32,pp. 42007–42020.

33. Basahel, S, Ali, T, Mostafa, M & Katabathini, N 2015, 'Influence of crystal structure of nanosized ZrO2 on photocatalytic degradation of methyl orange', Nanoscale Research Letters, vol.10, no.1,pp.1-13.

34. Mahadi Hasan, MD, Habib, MA, Prianka, S, Jannatul, N, Asish, KD, Ali, A & Nazmul Islam, AB 2021, 'Antioxidant, antibacterial and electrochemical activity of (E)-N-(4 (dimethylamino) benzylidene)-4H-1,2,4-triazol-4-amine ligand and its transition metal complexes', Results in Chemistry, vol.3, no.1, pp.100115-100121.